INTERVAL METHODS FOR THE IDENTIFICATION AND QUANTIFICATION OF INHOMOGENEOUS UNCERTAINTY IN HIGH-DIMENSIONAL MODELS: A TUTORIAL

Matthias Faes[1], David Moens[1]

[1] KU Leuven - Department of Mechanical Engineering
Jan De Nayerlaan 5, St.-Katelijne-Waver, Belgium
matthias.faes[at]kuleuven.be
david.moens[at]kuleuven.be

Key words: Inverse Uncertainty quantification, Interval methods, scarce data

Abstract. The quantification of inhomogeneous uncertain parameters in Finite Element models is a challenging task in case no direct measurement of these quantities is possible and when the available data are very scarce. In that case, classical probabilistic approaches such as Bayes' method might give unsatisfactory results due to necessary subjective assumptions. The authors recently introduced interval methods to cope with this situation by introducing an inverse approach to quantify interval field uncertain parameters, based on a limited set of indirect measurement data. These methods are based on the representation of the uncertainty in the responses of the structure as a convex set, and minimising the discrepancy between the convex set of the model responses and the convex set of replicated measurement data. This paper gives a brief overview of the recent developments and aims at giving a tutorial for the practical application of these new inverse methods.

1 INTRODUCTION

Interval Field Finite Element method were during the last decades introduced as an alternative to the well-established framework of probabilistic uncertainty representation. These methods are complementary to the probabilistic framework and are proven to provide objective estimates of the uncertainty in these models under scarce data, since the need for the identification of a full probabilistic data description is eliminated [1]. Interval fields were only recently introduced as an extension to this concept to account for non-homogeneous non-determinism, and can be regarded as a interval counterpart to the established framework of Random Fields [2]. The description of an interval field is based on the superposition of $n_b \in \mathbb{N}$ base functions $\boldsymbol{\psi}_i(\boldsymbol{r}) : \Omega \mapsto \mathbb{R}$, with $\boldsymbol{r}$ a spatial coordinate, scaled by independent interval scalars $\alpha_i^I \in \mathbb{IR}$, with $\mathbb{IR}$ the space of interval valued real numbers. The base functions $\boldsymbol{\psi}_i(\boldsymbol{r})$ represent a set of uncertainty patterns and describe the spatial nature of the uncertainty that is modelled by the interval field. The interval

scalars α_i^I capture the uncertainty at the input of the model. An interval field is formally expressed as:

$$\boldsymbol{\theta}^I(\boldsymbol{r}) = \sum_{i=1}^{n_b} \boldsymbol{\psi}_i(\boldsymbol{r})\alpha_i^I \tag{1}$$

However, in order to obtain a realistic model, an objective quantification of n_b, α_i^I and $\boldsymbol{\psi}_i(\boldsymbol{r})$ is needed. In case $\boldsymbol{x}$ is not measurable directly, as is for instance the case when contact stiffness values or component-level material properties are considered, such quantification is very challenging. The authors proposed a generic methodology for this identification. The method starts from a set of measurements of the system's responses, and represents the uncertainty in this measurements using set theoretical concepts. Similarly, also the uncertainty in the responses that is predicted by the interval field FE model is modelled. Then, the quantification of the interval field parameters consists of minimising the discrepancy between these two uncertain sets of responses. Also multiple extensions to the method were presented, as well as two reduction schemes. The complete overview can be found in [3–11]. This paper combines information from these publications and aims at giving a concise overview and practical tutorial of the complete methodology following a case-study approach.

2 INTERVAL FIELD FINITE ELEMENT ANALYSIS

Let $\mathcal{M}$ be a deterministic Finite Element model that is used to solve a (set of) differential equations for $\boldsymbol{z^m} \in \mathbb{R}^d$ through the vector valued function operator g:

$$\mathcal{M}(\boldsymbol{\theta}) : \boldsymbol{z^m} = g(\boldsymbol{\theta}), \qquad g : \mathbb{R}^k \mapsto \mathbb{R}^d \tag{2}$$

with $\boldsymbol{\theta} \in \mathcal{F} \subset \mathbb{R}^k$ the vector of model parameters and $\mathcal{F}$ the sub-domain of feasible parameters (e.g., non-negative contact stiffness).

The uncertainty that is attributed to $\boldsymbol{\theta}$ is modelled as an interval field $\boldsymbol{\theta}^I(\boldsymbol{r}) = \sum_{i=1}^{n_b} \boldsymbol{\psi}_i(\boldsymbol{r})\alpha_i^I \in \Omega \times \mathcal{F}^I$, with $\mathcal{F}^I \subset \mathbb{IR}^k$ and $\mathbb{IR}^k$ the space of k-dimensional interval vectors and Ω the model domain. Note that due to the orthogonality of all α_i^I, $i = 1, ..., k$, all interval scalars are independent by definition. In general the base functions satisfy $\int_\Omega \psi_i(\boldsymbol{r})\psi_j(\boldsymbol{r}) = \delta_{ij}$, but also non-orthogonal base functions can be applied [2]. Note that while the realisations of $\boldsymbol{\alpha}^I$ are located within a hyper-cubic subspace of $\mathbb{R}^{n_b}$, this is not the case for $\boldsymbol{\theta}^I(\boldsymbol{r})$, since $\boldsymbol{\psi}_i(\boldsymbol{r})$ provide a measure for the dependence [5].

The interval field FE method then searches solution set $\tilde{\boldsymbol{z}}^m$ containing the extreme realizations of $\boldsymbol{z^m}$ given the hyper-cubic parameter uncertainty in $\boldsymbol{\alpha}^I$. In general, $\boldsymbol{z^m}$ is not hyper-cubic, but spans a non-convex region in $\mathbb{R}^d$, since $\mathcal{M}$ provides coupling between z_i^m, $i = 1, ..., d$. Therefore, a direct and general solution to this problem is computationally intractable. As a result hereof, the solution set $\tilde{\boldsymbol{z}}^m$ is commonly approximated by an uncertain realization set $\tilde{\boldsymbol{z}}^m$, which is obtained by propagating q well selected deterministic realizations $\boldsymbol{z}_i^m$ of the hyper-cubic uncertain input parameters $\boldsymbol{\theta}^I$:

$$\tilde{\boldsymbol{z}}^m = \left\{ \boldsymbol{z}_i^m \mid \boldsymbol{z}_i^m = \mathcal{M}(\boldsymbol{\theta}_i); \boldsymbol{\theta}_i \in \boldsymbol{\theta}^I; i = 1, \ldots, q \right\} \tag{3}$$

These realisations can either stem from a global optimization approach [1] or dedicated sampling methods such as the Transformation Method [12, 13]. Alternatively, direct computation using affine arithmetical approaches are applied [14, 15].

3 INVERSE INTERVAL QUANTIFICATION

3.1 Interval field quantification procedure

The general overview of the procedure to quantify non-homogeneous uncertainty in FE models based on a set of scarce measurement data is illustrated in the workflow shown in figure 1.
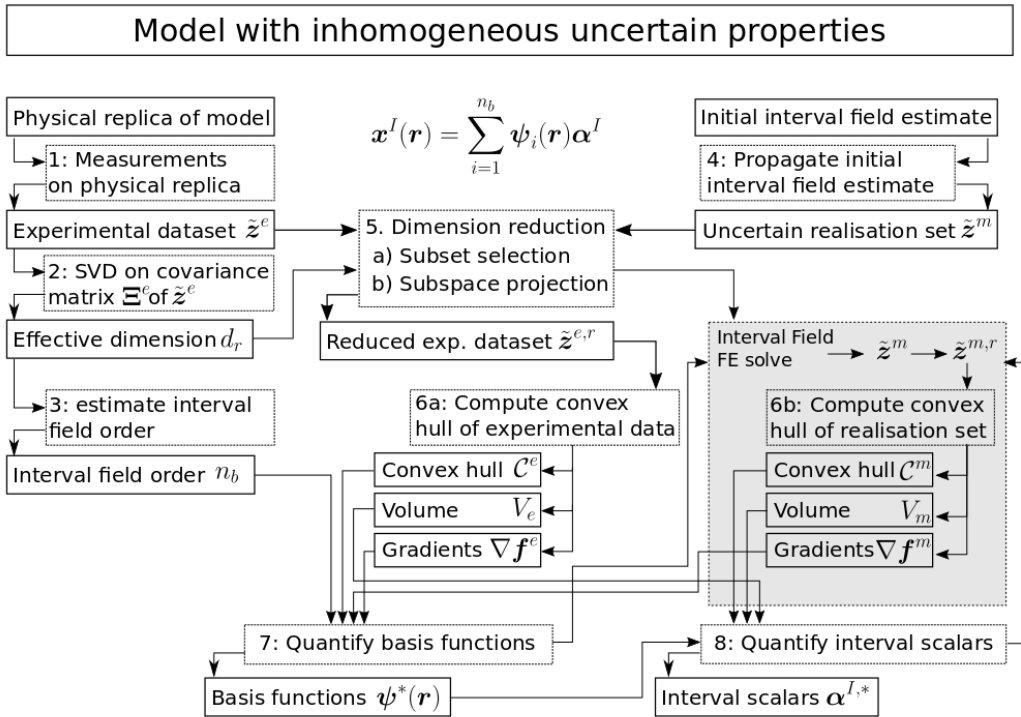
Figure 1: General overview of the methodology

The following paragraphs explain each step in detail. Furthermore, some illustrations are given to further explain some concepts. These illustrations are based on a numerical model that predicts the modal behaviour of a simple cantilever beam (figure 2), as described in [6]. The 10 first eigenmodes of this model are computed using an FE model with 10 4-node bilinear shell elements. It is considered that Young's modulus is subjected to spatial uncertainty. Measurement data of the 10 first eigenmodes are generated by sampling from a predefined interval field on Young's modulus. The presented methods are applied to quantify this pre-defined interval field using only the measured responses.

Step 1: The first step in the inverse quantification procedure consists of gathering and preparing the experimental data that is needed for the inverse quantification procedure
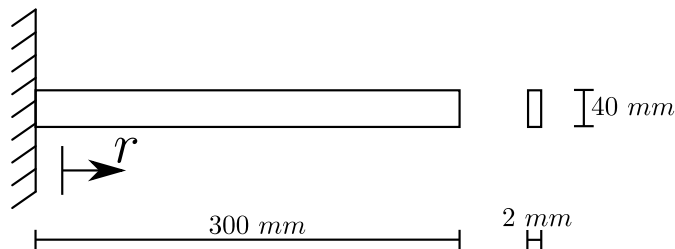
Figure 2: Illustration of the cantilever beam.

by performing t replicated experiments on a physical replica of the considered model. These measurements are then used to construct a measurement set $\tilde{\boldsymbol{z}}^e$. Then, the non-determinism that is present in these replicated measurements is bounded by its convex hull $\mathcal{C}^e$, which is formally defined as:

$$\mathcal{C}^e = \left\{ \sum_{j=1}^{t} \beta_j \boldsymbol{z}_j^e \mid (\forall j : \beta_j \geq 0) \wedge \sum_{j=1}^{t} \beta_j = 1 \; ; \; \boldsymbol{z}_j^e \in \tilde{\boldsymbol{z}}^e \right\} \qquad (4)$$

with β a vector of weighting factors, such that all elements β_j are non-negative and sum to one. Alternatively, it can also be represented as a set containing h_e d-dimensional half-spaces representing the linear inequalities that describe boundaries of $\mathcal{C}^e$:

$$\mathcal{C}^e \equiv \boldsymbol{A}_e (\boldsymbol{z}^e)^T - \boldsymbol{b}_e \geq 0 \qquad (5)$$

with $\boldsymbol{A}_e \in \mathbb{R}^{h_e \times d}$, $\boldsymbol{b}_e \in \mathbb{R}^{hee}$ and h_e the number of half-spaces that are needed to describe $\mathcal{C}^e$ [16]. The preprocessing of the data from different experiments in a dynamic FE model context is rather straightforward, as the analyst only has to keep track of eigenmode cross-over or -veering to ensure that the correct measured eigenfrequencies are compared. This can for instance be ensured by using MAC-based mode tracking [18].

The case of quasi-static models requires a bit more elaboration. Since widely applied techniques such as extensometers and strain gauges give only a very limited amount of spatial information on the occurring strains in a quasi-statically loaded specimen, it is rather cumbersome to quantify non-homogeneous uncertainty using these methods. Therefore, it was proposed to apply full-field strain measurements such as Digital Image Correlation (DIC) [9, 17] in this case as they provide strain data with very high spatial resolution containing up to $\mathcal{O}(10^{06})$ measurement points throughout Ω. These methods employ cameras to track the displacement of each location in Ω during loading to infer displacement and strain fields corresponding to each load step. However, two new specific challenges arise in this context:

1. The coordinate system (CS), in which the measured strains and displacements that are obtained using these techniques is in general not the same for all t measured replicas. This is a direct result from the practical difficulties associated with placing all tested specimens on the exact relative position with respect to the cameras in
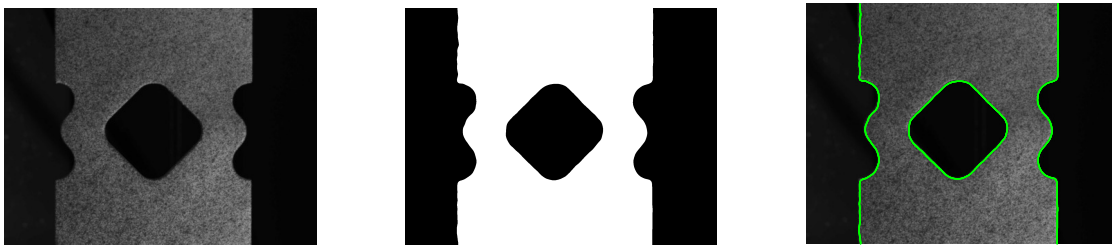
Figure 3: Illustration of the edge detection. Left: original image used in DIC; Middle: binarised image using Otsu's method; Right: detected edges in the original image via Laplacian edge detection

real testing environments. Moreover, these CS are also in general not coincident with the CS of the corresponding numerical model. This hinders an accurate comparison of the strain and/or displacement values stemming from the different tests and the numerical model throughout the model domain Ω. As such, an alignment procedure is needed to match (1) the CS of all measured replica $\boldsymbol{z}_j^e$ and (2) match these CS to the CS of the FE model under consideration.

2. The number of measured responses d is in general not the same for all $\boldsymbol{z}_j^e$ since DIC acts as a highly non-linear low pass filter in the spatial domain. Furthermore, d usually is also several orders of magnitude larger as compared to the number of responses that are given by the corresponding FE model. As such, each $\boldsymbol{z}_j^e$ has to be interpolated to the nodes of the FE model to ensure an accurate comparison.

In order to align the CS of all $\boldsymbol{z}_j^e$, $j = 1, \ldots, t$, one specimen with reference image f_{ref} is arbitrarily chosen from the set of measured replicas as a reference, and all other images f_i, $i = 1, ..., t-1$ of the tested specimens are aligned to this reference f_{ref}. In this way, also the corresponding displacement- and strain fields are aligned, as they are inherently connected to the images. The alignment is obtained by algorithmically detecting the edges of the specimens in the reference images using a combination of Otsu's method and Laplacian edge detection [18], and fitting these detected edges in a least-squares way by quantifying the complete image transformation matrix. The detection of the edges is illustrated in figure 3. The coordinate system of f_{ref} is then also aligned to the coordinate system of the numerical model.

In order to obtain a measured response that corresponds to the location of a computed response in the FE model, it is proposed to compute the average of all responses $\boldsymbol{z}_m(\boldsymbol{r}_{DIC})$ that are measured at a location $\boldsymbol{r}_{DIC}$ in the neighbourhood $\mathcal{N}(\boldsymbol{r}_{FE}) \subset \Omega$ of a node $\boldsymbol{r}_{FE,i}$ of the FE model:

$$\boldsymbol{z}_m(\boldsymbol{r}_{i,FE}) = \frac{1}{\mathcal{N}(\boldsymbol{r}_{i,FE})} \int_{\mathcal{N}(\boldsymbol{r}_{i,FE})} \boldsymbol{z}_m(\boldsymbol{r}_{DIC}) dr \qquad i = 1, ..., d \qquad (6)$$

As such, a measured response $\boldsymbol{z}_{mj}$ is obtained for each node i in Ω, located at $\boldsymbol{r}_{i,FE}$. The

notation $\boldsymbol{z}_m(\boldsymbol{r}_{i,FE})$ is used instead of the vector notation, in order to explicitly denote the correspondence of all measurement points that are contained in each replica $\boldsymbol{z}_m$ with a location in the model domain Ω. In case element responses (strains) are used for the comparison, the reduction of the measurement data set is straightforward, as $\mathcal{N}(\boldsymbol{r}_{FE}) \subset \Omega$ is considered to be coinciding with the elements of the FE discretization. On the other hand, when nodal response (displacements) values are used for the identification, $\mathcal{N}(\boldsymbol{r}_{FE})$ is constructed based on a mesh that connects the midpoints of the elements.

Step 2: The effective dimension of the experimental data set $\tilde{\boldsymbol{z}}^e$ is determined, based on the idea that the combination of d system responses not necessarily represents a d-dimensional manifold in $\mathbb{R}^d$, e.g. due to a high degree of dependence between certain responses. d_r is specifically determined using a singular value decomposition over the covariance matrix $\boldsymbol{\Xi}^e$ of $\tilde{\boldsymbol{z}}^e$:

$$\boldsymbol{\Xi}^{\boldsymbol{e}} = \boldsymbol{\Phi}^{\boldsymbol{e}} \boldsymbol{\Lambda}^{\boldsymbol{e}} (\boldsymbol{\Phi}^{\boldsymbol{e}})^T \qquad (7)$$

with $\boldsymbol{\Lambda} \in \mathbb{R}^{d \times d}$ the diagonal matrix of the ordered eigenvalues $\lambda_1 \leq \lambda_2 \leq \cdots \leq \lambda_d$ of $\boldsymbol{\Xi}$, and $\boldsymbol{\Phi} \in \mathbb{R}^{d \times d}$ a matrix containing the orthogonal eigenvectors $\boldsymbol{\phi}_j^e \in \mathbb{R}^d$, $j = 1, ..., d$. Finally, the *effective* dimensionality d_r of the convex hull of the measurement data set $\mathcal{C}^e$ is then defined such that:

$$\sum_{i=1}^{d_r} \frac{\lambda_i^e}{tr(\boldsymbol{\Xi}^e)} \geq 1 - \epsilon \qquad (8)$$

with $tr(\boldsymbol{\Xi}^e)$ the trace of the covariance matrix, and ϵ the approximation error, which should be a very small number. A thorough explanation is given in [5]. Figure 4 illustrates the convergence of ϵ with respect to d_r, when applied to experimental data sets containing 25 up to 1000 samples [5].
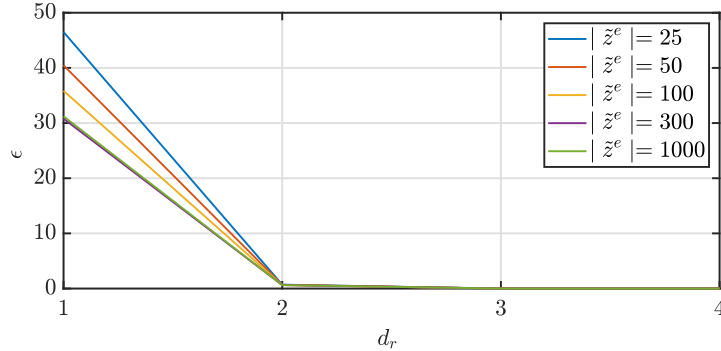
Figure 4: Convergence of ϵ with respect to d_r, when applied to experimental data sets containing 25 up to 1000 samples

Step 3: The correct number of base functions n_b corresponds with an uncertain realisation set $\tilde{\boldsymbol{z}}^m$ which has at least the same effective dimension as $\tilde{\boldsymbol{z}}^e$. Increasing n_b in eq. (1) increases the dimension of the hyper-cubic input space $\boldsymbol{\alpha}^I$. Furthermore, since more basis functions are defined, also the complexity of the coupling between local interval scalars

at each Ω_e. As such, n_b directly impacts d_r of $\tilde{z}^m$. In case of a strictly monotonic model $g()$, n_b can be chosen to be equal to d_r. For non-monotonic models n_b should be selected in an iterative approach [5].

Step 4: The initial guess on the parameters is mainly needed when gradient-based optimization algorithms such as Matlab's `fmincon` are used. Even in that case, it was shown in [6] that the obtained results are not sensitive to the initial estimate. When global optimisers are applied, this initial estimate is not used in the quantification procedure. In that case, rather the bounds between which the analyst believes that these parameters lie can be provided to speed up the algorithm.

Step 5: Two possible reduction schemes were presented recently by the authors since the computation of $\mathcal{C}^m$ and $\mathcal{C}^e$ scales exponentially with the number of considered responses. The first method, called the subset selection scheme [3, 6, 9] selects a subset of responses from the full uncertain realisation set containing the most informative responses, and as such retains the physical interpretation of the reduced convex hulls. As a drawback, this method requires forward solves of the interval field FE model. Alternatively, also the subspace projection method [5, 10, 11] was introduced. Instead of selecting an optimal subset of responses, the full uncertain realisation set and measurement data set are projected onto a lower dimensional basis, constructed via a singular value decomposition of the covariance matrix of the measurement data set. This method is completely objective with respect to the data and requires no forward FE solves. As a drawback, the method is rather sensitive to spurious data in the measurement data set, as the complete data set is considered. Therefore, appropriate data pre-processing is pre-emptive. Both methods will be explained in detail in the following:

Step 5a: The subset selection reduction scheme is originally presented in [6] and applied also in [9], and is based on the idea that a limited subset of the total response vector contains sufficient information to steer the quantification procedure. The performance of the method is also verified in [6, 9, 18]. Consider the index set $\mathcal{L}$, where each index l corresponds to a a combination of d_r responses out of the result vector $\boldsymbol{z}_i^m$, then following optimization problem determines the optimal subset:

$$l^* = \underset{l \in \mathcal{L}}{arg\,max} \left(\sum_{i=1}^{k} \left(\left| \frac{\partial V_{m,l}^r}{\partial r_{\alpha_i}} \cdot \frac{r_{\alpha_i}}{V_m} \cdot \frac{1}{\sum_l \frac{\partial V_{m,l}^r}{\partial r_{\alpha_i}} \cdot \frac{r_{\alpha_i}}{V_m}} \right| \cdot \frac{min(\boldsymbol{\Lambda}_c^r)}{max(\boldsymbol{\Lambda}_c^r)} \right) \right) \tag{9}$$

where l^* denotes the index number of the optimal subset $V_{m,l}^r$ is the multidimensional volume of the candidate reduced uncertain realisation set, r_{α_i} is the radius of one of the k locally defined interval scalars and V_m is the volume of the uncertain realisation set. $\boldsymbol{\Lambda}_c^r \in \mathbb{R}^{d_r \times d_r}$ represents the diagonal matrix containing the ordered d_r eigenvalues, as obtained by performing a singular value decomposition of the covariance matrix $\boldsymbol{\Xi}_c^r \in \mathbb{R}^{d_r \times d_r}$ of the candidate uncertain realisation set $\tilde{\boldsymbol{z}}_l^{m,r}$. Technically, the optimization problem can be solved by brute forcing the solution when the number

of responses is comparably low [6], or by using integer-valued genetic algorithms for larger FE models [9]. Both approaches were shown to be viable.

Step 5b: The subspace projection reduction scheme is originally presented in [5] and extended in [10,11]. Specifically, both $\tilde{\boldsymbol{z}}^m$ and $\tilde{\boldsymbol{z}}^e$ are projected onto a basis $\mathcal{B} \in \mathbb{R}^{d_r}$ before computing the convex hulls, which is defined as:

$$\mathcal{B} = \mathrm{span}\left(\boldsymbol{\phi}_{d-d_r}^e, \boldsymbol{\phi}_{d-d_r+1}^e, ... \boldsymbol{\phi}_d^e\right) \tag{10}$$

with d_r the effective dimension of $\tilde{\boldsymbol{z}}^e$ [5] and $\boldsymbol{\phi}_m$ are those eigenvectors in $\boldsymbol{\Phi}_m$ that correspond to the d_r largest eigenvalues in $\boldsymbol{\Lambda}_m$, and stem from the singular value decomposition presented in eq. (7). If d_r would be still too large to allow for computing $\mathcal{C}^e$ and $\mathcal{C}^m$, $\tilde{\boldsymbol{z}}^{m,r}$ and $\tilde{\boldsymbol{z}}^{e,r}$ are further projected onto d_r^+-dimensional subspaces, defined by a lower-dimensional orthogonal basis $\mathcal{B}_i^+ \subset \mathcal{B}$, $i = 1, \ldots, \binom{d_r}{d_r^+}$, constructed as a subset of $\mathcal{B}$, with $d_r^+ << d_r$ and $\binom{d_r}{d_r^+}$ the binomial coefficient [8,11]. Specifically, the ith orthogonal subspace basis $\mathcal{B}_i^+$ is defined as:

$$\mathcal{B}_i^+ = \{\boldsymbol{\phi}_{m,\mathcal{I}_i(1)}, \boldsymbol{\phi}_{m\mathcal{I}_i(2)}, \ldots \boldsymbol{\phi}_{m,\mathcal{I}_i(d_r^+)}\} \tag{11}$$

with $\mathcal{I}_i$ an index set containing the d_r^+ indices for the ith, $i = 1, ..., \binom{d_r}{d_r^+}$ subspaces of the vector space by $\mathcal{B}$. The convex hulls are then computed in each $\mathcal{B}_i^+$. This projection on sub-bases however comes at the cost of losing higher-order interaction between model responses. In the case of the AIRMOD test structure [19], a speed-up of the objective function evaluation with a factor 10^{05} was obtained [20] following this approach, while maintaining an accurate quantification of the uncertain parameters.

Note that where 5a is performed using the computed model responses, the reduction in 5b is solely based on the available measurement data.

Step 6a: For computational efficiency, $\mathcal{C}^e$ and its derivative quantities are computed prior to steps 7: and 8:, and passed to the optimization solvers where needed. The equations needed to perform these computations are given in the relevant step. Note that this computations are performed using the reduced experimental data set.

Step 6b: The computation of the convex hull of the realisation set and its derivative quantities are needed in each iteration of Step 7 and Step 8.

Step 7: The base functions $\boldsymbol{\psi}_i(\boldsymbol{r})$ that model the spatial nature of $\boldsymbol{\theta}^I(\boldsymbol{r})$ that is being quantified, are determined by minimising a squared $\mathcal{L}_2$ norm over the difference between the gradients of the half spaces that bound $\mathcal{C}^e$ and $\mathcal{C}^m$. Formally, the objective function is defined as:

$$\delta_{BV} = \left\| \nabla \boldsymbol{f}^m \left(\boldsymbol{\alpha}^I, \boldsymbol{\psi}_j(\boldsymbol{r})\right) \big|_{\boldsymbol{\alpha}^I = \boldsymbol{\alpha}_0^I} - \nabla \boldsymbol{f}^e \right\|_2^2 \tag{12}$$

where $\boldsymbol{f}^m$ is defined by considering only the crisp boundary of $\mathcal{C}^m$ and stems directly from following set of linear inequalities:

$$\boldsymbol{f}^m \left(\boldsymbol{\alpha}^I, \boldsymbol{\psi}(\boldsymbol{r})\right) = [f_1^m, f_2^m, ..., f_{h_m}^m]^T = \boldsymbol{A}_m \boldsymbol{z}^T - \boldsymbol{b}_m = \boldsymbol{0} \tag{13}$$

with $\forall f_i, i = 1, ..., h_s : \mathbb{R}^{d_r} \mapsto 0$. These functions are analogously defined for the measurement data set. The rationale behind this objective function is presented in [5] and also applied in [10], where it is shown that these gradients in fact contain information on the dependence between the intervals that are defined at each element of the FE model. This dependence stems directly from the base functions, as these interpolate the n_b globally defined interval scalars α_i^I towards intervals at each of the k elements in Ω. As such, $\nabla \boldsymbol{f}^e$ contains information on the local dependence of the uncertainty at the element level of the FE model, and hence, the correct basis functions. Furthermore, when $\boldsymbol{\psi}_j(\boldsymbol{r})$ is defined using inverse distance weighting interpolation [6], the optimization problem reduces to finding the correct control points [5]. Note that for each step in the iterative solution of this minimisation, subroutine $6b$: should be performed to compute $\mathcal{C}^m$ and $\nabla \boldsymbol{f}^m$.

Step 8: As a final step, the interval scalars are also quantified via an optimization approach. The objective $\delta(\boldsymbol{\alpha}^I)$ describes the discrepancy in volume between $\tilde{\boldsymbol{z}}^m$ and $\tilde{\boldsymbol{z}}^e$, and is defined as:

$$\delta(\boldsymbol{\alpha}^I) = \left(\Delta V_e^2 + \Delta V_o^2 + \Delta c^2\right) \tag{14}$$

with:

$$\Delta V_e = 1 - \frac{V_m(\boldsymbol{\alpha}^I)}{V_e} \tag{15a}$$

$$\Delta V_o = 1 - \frac{V_o(\boldsymbol{\alpha}^I)}{V_e} \tag{15b}$$

$$\Delta c = \left\| \boldsymbol{c}_e - \boldsymbol{c}_m(\boldsymbol{\alpha}^I) \right\|_2 \tag{15c}$$

with $\boldsymbol{c}_e$ and $\boldsymbol{c}_m$ the geometrical centres of mass of respectively $\tilde{\boldsymbol{z}}^e$ and $\tilde{\boldsymbol{z}}^m$. V_o is the multidimensional volume of the overlap $\tilde{\boldsymbol{z}}_o$ between $\tilde{\boldsymbol{z}}^e$ and $\tilde{\boldsymbol{z}}^m$, which is computed as the intersection between these two sets:

$$\tilde{\boldsymbol{z}}_o(\boldsymbol{\alpha}_j^I) = \mathcal{C}^m(\boldsymbol{\alpha}_j^I) \cap \mathcal{C}^e \tag{16}$$

In practice, $\tilde{\boldsymbol{z}}_o(\boldsymbol{\alpha}_j^I)$ can be determined as:

$$\tilde{\boldsymbol{z}}_o = \left\{ \boldsymbol{z}_j \mid \boldsymbol{A}_o \boldsymbol{z}_j^T - \boldsymbol{b}_o^T \le 0 \wedge \boldsymbol{z}_j \in \mathbb{R}^d \right\} \tag{17}$$

with $\boldsymbol{A}_o \in \mathbb{R}^{(h_m + h_s) \times d}$:

$$\boldsymbol{A}_o = [\boldsymbol{A}_m; \boldsymbol{A}_e]^T \tag{18}$$

and $\boldsymbol{b}_o \in \mathbb{R}^{(h_m + h_e)}$:

$$\boldsymbol{b}_o = [\boldsymbol{b}_m; \boldsymbol{b}_e]^T \tag{19}$$

with $\boldsymbol{A}_m \in \mathbb{R}^{h_m \times d}$, $\boldsymbol{A}_s \in \mathbb{R}^{h_s \times d}$, $\mathbf{b}_s \in \mathbb{R}^{h_s}$ and $\mathbf{b}_m \in \mathbb{R}^{h_m}$.

This optimization problem can be solved using gradient-based optimisers when a sufficiently accurate initial estimate is possible [6]. Otherwise, also global algorithms such as Particle Swarm Optimisation were shown to provide accurate results [11, 20]

Final result: The result of the quantification of the interval field on the case study is illustrated in figure 5. Based on the numerically generated measurement data, n_b, $\boldsymbol{\psi}(\boldsymbol{r})$ and $\boldsymbol{\alpha}^I$ were quantified according to the algorithms illustrated in figure 1 and the steps listed above. As can be seen, the method is capable of reconstructing the interval field that was used for the generation of the measurement data completely (denoted "$\boldsymbol{\theta}^I(\boldsymbol{r})$ measurement"). For a more thorough study of the performance of the methods using this case study, as well as more challenging examples, the reader is referred to [5, 6, 11]. In the referred papers, it is shown that for this specific case, both the subset selection as the subspace projection reduction schemes enable an accurate quantification of the uncertainty.
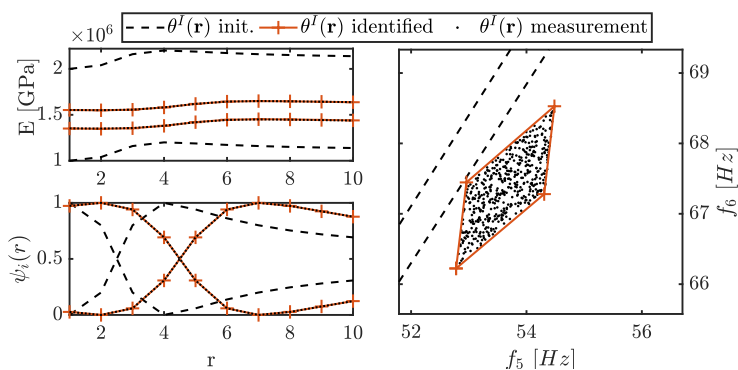
Figure 5: Illustration of the interval field quantification procedure

4 CONCLUSIONS

The quantification of spatial uncertainty of parameters that are not directly measurable is a challenging task, especially when only limited data are available. Recently, the authors presented an approach to tackle this problem using a combination of interval fields and set-theoretical approaches. This paper gives an overview of these developments, and is aimed at aiding the implementation of these new methods. A small scale example is used to illustrate several steps of the new method, and shows that a highly accurate quantification of the spatial uncertainty is possible. Future work will be focussed on expanding the scope of this method towards more generalised models of uncertainty such as imprecise probabilities, as well as applying these methods in case studies such as composite structures or additive manufacturing.

ACKNOWLEDGEMENTS

REFERENCES

[1] D. Moens and M. Hanss, "Non-probabilistic finite element analysis for parametric uncertainty treatment in applied mechanics: Recent advances," *Finite Elements in*

Analysis and Design, vol. 47, no. 1, pp. 4–16, 2011.

[2] W. Verhaeghe, W. Desmet, D. Vandepitte, and D. Moens, "Interval fields to represent uncertainty on the output side of a static FE analysis," *Computer Methods in Applied Mechanics and Engineering*, vol. 260, no. 0, pp. 50–62, 2013.

[3] M. Faes, J. Cerneels, D. Vandepitte, and D. Moens, "Identification of Interval Fields for Spatial Uncertainty Representation in Finite Element Models," in *Proceedings of the VII European Congress on Computational Methods in Applied Sciences and Engineering (ECCOMAS Congress 2016)*, vol. 3, pp. 6091–6098, 2016.

[4] M. Faes, J. C. D. Vandepitte, and D. Moens, "Quantification of interval field uncertainty in dynamic Finite Element models," *ISMA2016 International Conference on Noise and Vibration Engineering & USD2016 International Conference on Uncertainty in Structural Dynamics*, pp. 4347–4362, 2016.

[5] M. Faes and D. Moens, "Identification and quantification of spatial interval uncertainty in numerical models," *Computers and Structures*, vol. 192, pp. 16–33, 2017.

[6] M. Faes, J. Cerneels, D. Vandepitte, and D. Moens, "Identification and quantification of multivariate interval uncertainty in finite element models," *Computer Methods in Applied Mechanics and Engineering*, vol. 315, pp. 896–920, 2017.

[7] M. Faes, J. Cerneels, D. Vandepitte, and D. Moens, "Influence of measurement data metrics on the identification of interval fields for the representation of spatial variability in finite element models," *PAMM*, vol. 16, no. 1, pp. 27–30.

[8] M. Faes, D. Vandepitte, and D. Moens, "Identification and quantification of multivariate possibilistic manufacturing uncertainty in dynamic numerical models," in *Proceedings of the 2nd International Conference on Uncertainty Quantification in Computational Sciences and Engineering*, 2017.

[9] M. Faes and D. Moens, "Identification and quantification of spatial variability in the elastostatic properties of additively manufactured components," in *19th AIAA Non-Deterministic Approaches Conference*, no. January, pp. 1–13, 2017.

[10] M. Faes and D. Moens, "Quantification of non-homogeneous interval uncertainty based on scatter in modal properties," in *Procedia Engineering*, vol. 199, 2017.

[11] M. Broggi, M. Faes, E. Patelli, Y. Govers, D. Moens, and M. Beer, "Comparison of Bayesian and Interval Uncertainty Quantification: Application to the AIRMOD Test Structure," in *SSCI 2017*, 2017.

[12] M. Hanss, "The transformation method for the simulation and analysis of systems with uncertain parameters," *Fuzzy Sets and Systems*, vol. 130, pp. 277–289, sep 2002.

[13] M. Hanss, "The extended transformation method for the simulation and analysis of fuzzy-parameterized models," *International Journal of Uncertainty, Fuzziness and Knowledge-Based Systems*, vol. 11, pp. 711–727, dec 2003.

[14] D. Degrauwe, G. Lombaert, and G. D. Roeck, "Improving interval analysis in finite element calculations by means of affine arithmetic," *Computers & Structures*, vol. 88, no. 34, pp. 247 – 254, 2010.

[15] G. Muscolino and A. Sofi, "Bounds for the stationary stochastic response of truss structures with uncertain-but-bounded parameters," *Mechanical Systems and Signal Processing*, vol. 37, no. 1, pp. 163–181, 2013.

[16] H. Weyl, "Elementare Theorie der konvexen Polyeder," *Comentarii Mathematici Helvetici*, vol. 7, no. 1, pp. 290 – 306, 1934.

[17] P. Lava, S. Cooreman, S. Coppieters, M. De Strycker, and D. Debruyne, "Assessment of measuring errors in DIC using deformation fields generated by plastic FEA," *Optics and Lasers in Engineering*, vol. 47, pp. 747–753, jul 2009.

[18] M. Faes, *Interval methods for the identification and quantification of inhomogeneous uncertainty in Finite Element models.* PhD thesis, KU Leuven, Department of Mechanical Engineering, 2017.

[19] Y. Govers, H. Haddad Khodaparast, M. Link, and J. E. Mottershead, "A comparison of two stochastic model updating methods using the DLR AIRMOD test structure," *Mechanical Systems and Signal Processing*, vol. 52-53, pp. 105–114, jul 2015.

[20] M. Faes, M. Broggi, E. Patelli, Y. Govers, J. E. Mottershead, M. Beer, and D. Moens, "A multivariate interval approach for inverse uncertainty quantification with limited experimental data," *paper under review*, 2018.